Thermal transport through the magnetic martensitic transition in Mn$_x$MGe (M = Co, Ni)

Qiye Zheng,[1*†] Shannon E. Murray,[1†] Zhu Diao,[1,2,3] Ankita Bhutani,[1] Daniel P. Shoemaker,[1] and David G. Cahill[1]

[1]*Department of Materials Science and Engineering, Frederick Seitz Materials Research Laboratory, University of Illinois at Urbana-Champaign, 104 South Goodwin, Urbana, IL, USA 61801*

[2]*Department of Physics, Stockholm University, SE-106 91 Stockholm, Sweden*

[3]*School of Information Technology, Halmstad University, P.O. Box 823, SE-301 18 Halmstad, Sweden*

Abstract

We report on changes in the thermal conductivity of solid-state synthesized Mn$_x$MGe (M = Co, Ni, $0.98 < x < 1.02$) alloys through their temperature-induced martensitic structural transition. The thermal conductivity is measured by time-domain thermoreflectance (TDTR). Mn$_{1.014}$NiGe exhibits an increase in thermal conductivity from 11 to 15.5 W m^{-1} K^{-1} from approximately 575 K to 625 K; and Mn$_{1.007}$CoGe exhibits an increase in thermal conductivity from 7 to 8.5 W m^{-1} K^{-1} from 500 K to 550 K. In Mn$_x$NiGe, the transition temperature and the magnitude of the change in thermal conductivity are strongly dependent on the alloy composition. Our study advances fundamental understanding of the thermal transport properties in Mn$_x$MGe (M = Co, Ni) family of alloys and opens a new direction in the search for solid-state phase transition materials with potential applications as thermal regulators.

Introduction

Thermal regulator materials, i.e., materials that have a reversible abrupt transition from a low to high thermal conductivity state upon heating, are potentially useful for maintaining an optimal

---

* Qzheng9@illinois.edu
† Contribute equally to the work.

temperature of an engineering system and therefore improve its efficiency. For example, in modern automobiles, the average fuel conversion efficiency of an internal combustion engine is approximately 35-40% [1]. However, the engine efficiency is only ~10% while warming from ambient temperature to the optimal operating temperature of 373 K [1,2]. A reduction in the warm-up time for an engine without risking overheating could improve overall efficiency and reduce the emission of harmful exhaust gasses [3]. Thermal regulator materials are potentially a convenient approach for solving this thermal management problem.

However, a high contrast change of thermal conductivity in a narrow temperature window is rarely found in materials. Thermal conductivity typically changes gradually [4-11]. Additionally, the high temperature phase rarely has a higher thermal conductivity than the low temperature phase. Notable exceptions are the metal–insulator transition (MIT) in some transition metal oxides (e.g., VO_2, Ti_2O_3, and $La_{1-x}Sr_xCoO_3$) and the martensitic transition (MT) in some alloys [12-17]. Although MIT oxides possess a large increase in electrical conductivity, the metallic phase thermal conductivity is still low, e.g., ≈ 6 W m^{-1} K^{-1} in VO_2 [15,18].

The goal of this work is to discover and study novel solid phase transition intermetallic materials with thermal regulating behavior, i.e., a transition from low to high thermal conductivity state as temperature rises, at temperatures above 300 K.

To begin, we used the Materials Project database to search for ternary metallic or intermetallic compounds that are known to exist in at least two phases [19]. After narrowing the list of candidates to compounds where the structural transition occurs as a function of temperature below 900 K, we identified the TiNiSi-type family of compounds, which includes MnCoGe and MnNiGe, as exhibiting metallic characteristics with tunable chemistry and transition temperatures.

2

As members of MM′X family of compounds [20-22], MnCoGe and MnNiGe exhibit both a martensitic structural transition and a magnetic transition. The stoichiometric MnCoGe alloy transforms between the low temperature TiNiSi-type orthorhombic (*Pnma*), martensite phase and the high temperature Ni_2In-type hexagonal ($P6_3/mmc$), austenite phase via a MT near 420 K [23]. Stoichiometric MnNiGe transforms between these two phases at 470 K [23]. MnCoGe also possesses a ferromagnetic to paramagnetic transition with a Curie temperature of $T_C \sim 345$ K [21,24]. In MnNiGe, the analogous transition between antiferromagnetic and paramagnetic order occurs at a Néel temperature of $T_N \approx 346$ K [21,24]. Both materials can be synthesized through solid state methods [23].

In metallic alloys, the martensitic transformation (MT) sometimes results in a strong modification of the Fermi-level electron density of states and electron mobility. The result is a change in the electrical resistivity and electronic thermal conductivity [25,26]. For example, a number of Heusler alloys and shape memory alloys possess anomalies in their electrical transport properties attributed to the MT [17,27-29]. In Ni-Mn-X (X = In, Ga) Heusler alloys, a reduction of the electrical resistivity from the martensite to the austenite phase leads to an increase of thermal conductivity upon heating across the MT. The change in thermal conductivity across the MT is around 50-60%, in Ni-Mn-In off-stoichiometric alloys, while <5% in Ni_2MnGa (see the discussion section for a detailed comparison) [30-33]. The Ni-Ti alloys also show larger thermal conductivity in the austenite phase, ≈ 15 W m^{-1} K^{-1} near 300 K, with the contrast in thermal conductivity across the MT around 15% resulting from the electron contribution [27]. A decrease in the electrical resistivity upon heating across the MT has been reported in a powder composite sample of $MnCoGe_{0.985}In_{0.015}$ bonded with 3.9 wt % epoxy binder [20]. Whether the electronic contribution dominates the thermal conductivity in MnCoGe and MnNiGe remains unresolved.

Here, we report a time-domain thermoreflectance (TDTR) study of the temperature dependent thermal conductivity in nearly stoichiometric Mn_xMGe (M = Co, Ni, $0.98 < x < 1.02$) alloys, synthesized by solid state methods, through the martensitic and magnetic phase transitions. Their composition, structure, and transition temperatures are characterized using X-ray fluorescence (XRF), X-ray diffraction (XRD), magnetometry and differential scanning calorimetry (DSC). We observed an increase in the thermal conductivity in both alloys across the martensitic transition upon heating. The magnitude of the change of thermal conductivity and the transition temperature are dependent on the alloy composition. The thermal conductivity of Mn_xNiGe in the high temperature phase (13 to 16 W m^{-1} K^{-1} at 600 K) is larger than common MIT oxides such as VO_2, and comparable to stainless steel and some of the aluminum alloys used in internal combustion engines [10,34]. Using infrared spectroscopy, the dc electrical resistivity of the alloys is inferred to be approximately 470 and 680 $\mu\Omega$ cm for Mn_xCoGe and Mn_xNiGe, respectively. The relatively large electrical resistivities indicate that phonons make a larger contribution to the total thermal conductivity than electrons. This work identifies new materials exhibiting thermal regulating behavior with higher thermal conductivities at high temperatures and provides novel knowledge about the thermal transport properties in Mn_xMGe family of alloys.

Experimental

Sample preparation

Mn_xNiGe and Mn_xCoGe were synthesized by solid state methods following a procedure adapted from that described by Johnson [23]. For Mn_xNiGe, Mn (99.98% purity), Ni (99.999% purity), and Ge (99.999% purity) powders were combined in the appropriate ratios in an argon (Ar)-filled glovebox. Excess Mn was added to compensate for Mn loss during firing. We also

varied the Mn content intentionally to study the compositional dependence of the martensitic transition temperature and to obtain samples with MT temperatures above 300 K but not exceeding the temperature limit of TDTR (the commonly used Al transducer layer for TDTR degrade at > 700 K). The powders were placed in alumina crucibles within quartz tubes to avoid reaction between the powder and the quartz tube. The tubes were evacuated and sealed. Samples were fired for 16 hours at 1248 K and cooled to room temperature at 2 K/min. The tubes were then opened in the glovebox, the powder was ground, and the tube was resealed. A second firing was performed for two hours at 1373 K, followed by 16 hours at 973 K, and then cooled at 10 K/min to room temperature. The second firing and additional grinding was necessary to achieve homogenous samples. All heating rates were 10 K/min. Mn_xCoGe samples were synthesized by the same method using Co (99.95% purity) powder.

To prepare a smooth surface for thermal conductivity measurements by time-domain thermoreflectance, the Mn_xMGe chunks were mechanically polished. Prior to polishing, irregularly shaped pieces, on the scale of a few millimeters, were imbedded in Crystalbond® adhesive. Following polishing, the samples were removed from the Crystalbond® by sonicating in acetone. The chunks were also rinsed in IPA and ethanol to remove any remaining residue. The samples were then coated with Al by dc magnetron sputtering. We measured smooth regions with >95% of the reflectivity of a reference commercial Si wafer coated with Al by the same sputtering process.

Characterization

Powder X-ray diffraction (XRD) data of the final product (after the second firing) were collected on a Siemens D5000 diffractometer with a Cu-Kα source in reflection geometry. This geometry avoids the X-ray absorption problems of the transmission geometry. Rietveld

refinements of all XRD data were carried out using TOPAS 5. In-situ XRD scans were collected on a Bruker D8 ADVANCE diffractometer in a transmission geometry using a Mo-Kα source and LYNXEYE XE detector. A TC-Transmission® capillary stage with an oven was used to heat the sample. The sample was sealed within two quartz capillaries. The inner 0.3 mm diameter quartz capillary was sealed under vacuum to avoid exposing the sample to oxygen while at high temperatures. The second 0.7 mm diameter quartz outer capillary provided support and allowed the sample to attach to the stage. The samples were heated 5 K between scans then held at a constant temperature during the scan. The heating and cooling rates between scans were both 10 K/min. All of the XRD data included in this publication were taken after the second firing of the samples.

X-ray fluorescence (XRF) data were collected using a Shimadzu EDX-7000 spectrometer. Quantitative scans were performed under a helium atmosphere. The entire sample that was synthesized was placed in the sample holder. Four sets of data were averaged to determine the composition. Between each data collection, the sample holder was "shaken" (inverted and righted multiple times) to detect a larger volume fraction of the sample. The results of the four runs were averaged and their standard deviation has been used as the error bars in all plots of x. For all Mn_xNiGe samples, the standard deviation of x is 0.009 moles or smaller (e.g., sigma ≈0.004 moles for $x = 0.981$). Therefore, the Mn composition, x, has been listed to the thousandths place in this work. The composition of the ternary phase cannot be accurately determined using XRF when a second phase is present as XRF only provides the average composition of a sample. Samples found to have phase separation between the ternary phase and Mn using scanning electron microscopy and energy dispersive spectroscopy were not included in the following analysis.

Differential scanning calorimetry (DSC) data were collected using a TA Instrument DSC Q20. Samples were ground into powder and hermetically sealed in aluminum sample pans in an Ar - filled glovebox. The samples were heated from 193 to 823 K and cooled back to 193 K with ramps of 20 K/min under flowing Ar (50 mL/min). Equilibration at the maximum and minimum temperatures was performed, followed by 5-minute isothermal holds.

Temperature dependent magnetization measurements were carried out using a superconducting quantum interference device (SQUID) magnetometer (Quantum Design Magnetic Property Measurement System MPMS® 3).

We used time-domain thermoreflectance (TDTR) to measure the thermal conductivity of Mn_xMGe [35,36]. In a TDTR measurement, a train of optical pulses at a repetition rate of 80 MHz, generated by a mode-locked Ti:Sapphire laser at a wavelength of 785 nm, is split into separate pump and probe beams with the optical path of the pump beam controlled by a mechanical delay stage. The pump beam is modulated at a frequency of 9.1 MHz by an electro-optical modulator. The pump and probe beams are focused on the sample through a 5× objective lens to a $1/e^2$ intensity radius of ≈10.7 μm. The total beam power of 15 mW creates a steady-state temperature rise of <9 K at room temperature and <7 K at 600 K. The changes in the intensity of the reflected probe beam created by the pump beam are measured using phase-sensitive lock-in detection. The ratio of the in-phase (V_{in}) and out-of-phase (V_{out}) signal from the lock-in amplifier is then fit to a thermal diffusion model obtained from an analytical solution for heat flow in a layered structure [35].

Temperature-dependent TDTR measurement from 300-600 K are performed by mounting the specimen on a commercial Instec® heater stage in a vacuum chamber and monitoring the sample temperature with a Pt resistance thermometer. To minimize sample oxidation, the chamber is

pumped with a turbo-molecular pump to maintain a pressure lower than 7.5×10^{-4} Torr at high temperature.

In the TDTR data fitting, the thermal transport model used for fitting includes parameters for the thermal conductivity, heat capacity, and thickness of the Al transducer layers and the Mn_xMGe sample. The thickness of Al thin film was obtained from picosecond acoustics using a longitudinal speed of sound of 6.42 nm/ps [37]. The thermal conductivity of the Al thin film was calculated using the Wiedemann-Franz law and the electrical resistance of the same transducer layer deposited on a 500 nm SiO_2 on Si reference sample. The analysis is not sensitive to the Al thermal conductivity: a 40% error in the Λ_{Al} propagates into only an $\approx 1\%$ error in the thermal conductivity of the sample. The heat capacity of Al is taken from literature values [38].

Analysis of TDTR data for thermally-thick samples requires knowledge of the volumetric heat capacity, C, of the sample. At room temperature and above, the classical Dulong-Petit law, $C = 3Nk_B$ where N is the atomic density and k_B is the Boltzmann constant, often provides an estimate of C that has smaller uncertainties than the other uncertainties in the measurement. For Mn_xMGe, $3Nk_B = 3.1$ J cm^{-3} K^{-1}. This result is close to the value of 3.15 J cm^{-3} K^{-1} measured for $Mn_{1-x}Fe_xCoGe$ (x < 0.2) and 3.2 J cm^{-3} K^{-1} for $(MnCo)_{1-x}Ge$ (x = 0.02) at 300 K [39,40]. While C will have some temperature dependence over the temperature range of our measurements (300-600 K), we elected to fix the volumetric heat capacity in the data analysis at 3.2 J cm^{-3} K^{-1} to reduce the complexity of the data analysis. Since the Debye temperature of Mn_xMGe should be comparable to 300 K [39], we expect that any changes in the volumetric heat capacity with temperature are smaller than the uncertainties in the measurement $\approx 5\%$. In addition, the change in heat capacity between the two phases at the vicinity of the MT is also small, < 3% [40],

The thermal conductivity of the Mn_xMGe sample and the thermal conductance of the Al/alloy interface, G, are the only two parameters that are adjusted for curve fitting. G is measured to be 80 to 120 MW m^{-2} K^{-1} in these alloys, typical for Al/metal interfaces with nanometer-thin surface oxides. TDTR measurements of thermal conductivity are discussed extensively below.

Infrared reflectance spectra of the Mn_xMGe samples were studied using a Vertex 70 Fourier transform infrared spectrometer coupled to a Bruker Hyperion microscope. We used a 15x objective lens (N.A. = 0.4) with a 1.8 mm aperture at the back focal plane. A KBr beamsplitter was used for the measurement of the mid infrared spectra. A Newport® broadband metallic mirror with gold coating was used as a reference in the FTIR measurement.

Results
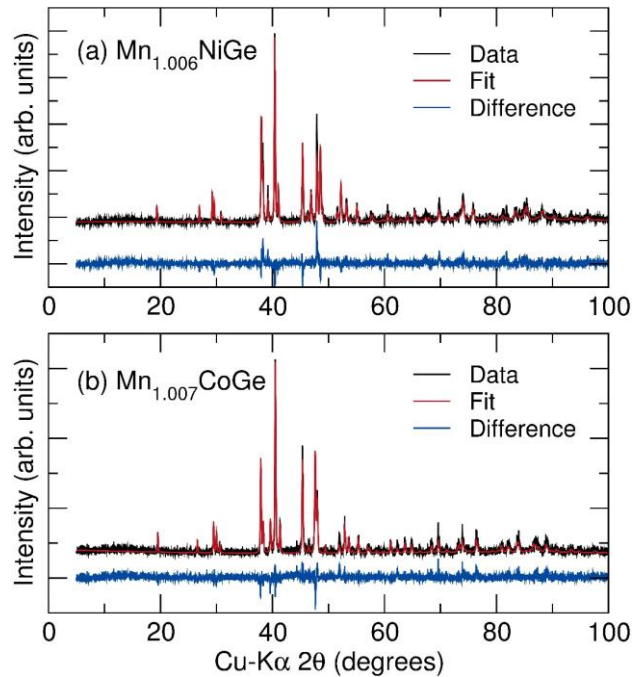
FIG. 1. Representative room temperature, ex-situ X-ray diffraction data and Rietveld refinements of $Mn_{1.006}NiGe$ and $Mn_{1.007}CoGe$. The difference between the data (black curves) and the refinement fit (red curves) is shown as blue curves.
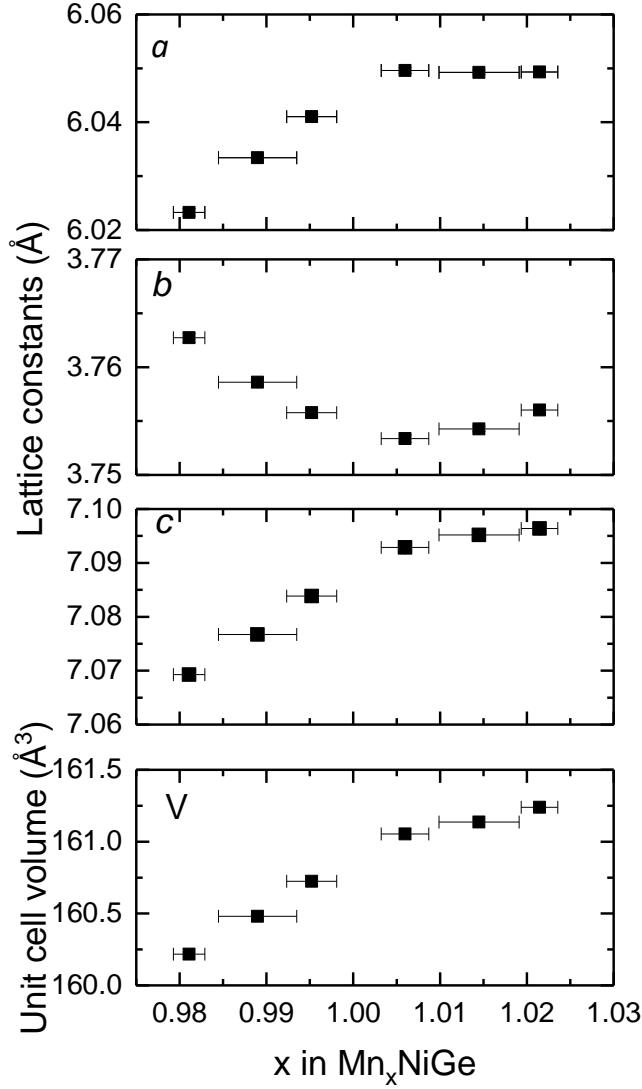
FIG. 2. Lattice parameters and unit cell volume of the Mn_xNiGe compounds obtained from room temperature X-ray diffraction. The lattice parameters plateau as the Mn content increases past x ≈1.01, indicating a potential limit to the doping of Mn_xNiGe with Mn. The x-axis error bars are the standard deviation of four X-ray fluorescence runs. The y-axis error bars are smaller than the symbols and cannot be seen.

Room temperature, ex-situ XRD scans were taken for each sample to confirm the purity and phase. Representative Rietveld refinement results are shown in Fig. 1 for both Mn_xMGe (M = Co, Ni) systems. Both $Mn_{1.006}NiGe$ and $Mn_{1.007}CoGe$ are fit using their respective orthorhombic structures. The difference (blue) curves show that no peak is unaccounted for. All the Mn_xNiGe

and Mn_xCoGe samples are orthorhombic at room temperature. Additionally, using ex-situ XRD, the room temperature lattice parameters of the Mn_xNiGe compounds were determined, as summarized in Fig. 2. ZnO powder was mixed as a standard for improved accuracy. The x-axis error bars are the standard deviation of four X-ray fluorescence runs. The y axis error bars are smaller than data symbols. Lattice constants of *a* and *c* increase while *b* first decreases then increases with increasing Mn content. All three lattice parameters and the unit cell volume show a change of slope and tend to plateau as the amount of Mn is increased past $x \approx 1.01$. Such behavior indicates a potential limit to doping Mn_xNiGe with Mn at even higher *x*.

The thermally-driven transformations in Mn_xMGe (M = Co, Ni) were confirmed using in-situ XRD. This technique provides the structural transition temperature of the material, as well as the low and high temperature phases. The transformation of $Mn_{1.021}NiGe$ between orthorhombic and hexagonal phases upon both heating and cooling are shown in Fig. S1.
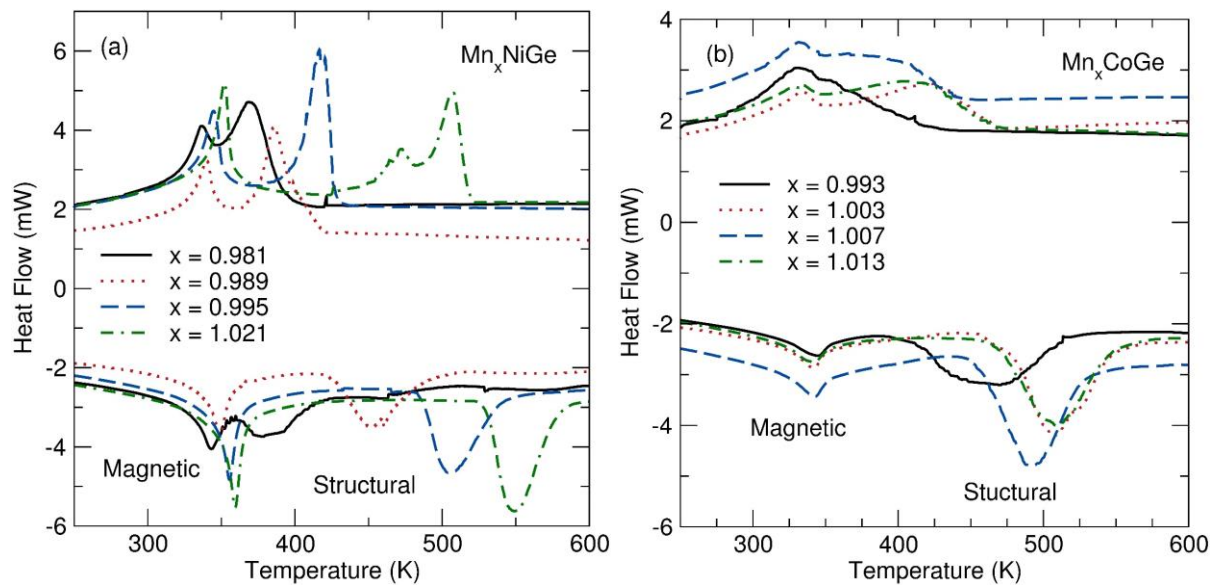
FIG. 3. Differential scanning calorimetry data of the (a) Mn_xNiGe and (b) Mn_xCoGe system upon heating and cooling with ramps of 20 K/min between 193 and 800 K (only data between 250 and 600 K are shown). The magnetic and structural transition temperatures are labeled; the magnetic transition occurs at lower temperature than the structural transition. The magnetic and structural transition temperatures in general increase with the Mn content

The structural and magnetic transition temperatures are more accurately obtained using DSC from the endothermic and exothermic peaks upon heating and cooling (between 193 and 800 K with ramps of 20 K/min), respectively. We show representative data for the Mn_xNiGe and Mn_xCoGe samples in Fig. 3 (a) and (b), respectively. Upon heating, the endothermic peaks corresponding to the magnetic transition temperatures appear first, closely clustered around 350 K in agreement with previous reports [41,42]. These peaks were confirmed to be associated with the magnetic transition by SQUID magnetometry measurements, as shown in Fig. 4 and described below. Upon further heating, structural transitions appear as endothermic peaks in both Mn_xNiGe and Mn_xCoGe samples, in agreement with in-situ XRD data (Fig. S1), and prior reports [21,23,42].

In Mn_xNiGe, both the magnetic and structural transition temperatures increase with x. The structural transition occurs in a temperature range over ~200 K indicating the properties are highly dependent on the amount of Mn. Hysteresis, shown by DSC, is present in the structural transition temperature with a magnitude that decreases with x (also see Fig. 5). The magnetic transition shows significantly less hysteresis and a much smaller peak width compared to the structural transition. The properties of Mn_xCoGe are much less dependent on the Mn content with peaks corresponding to the structural transitions clustered in a much narrower temperature range.
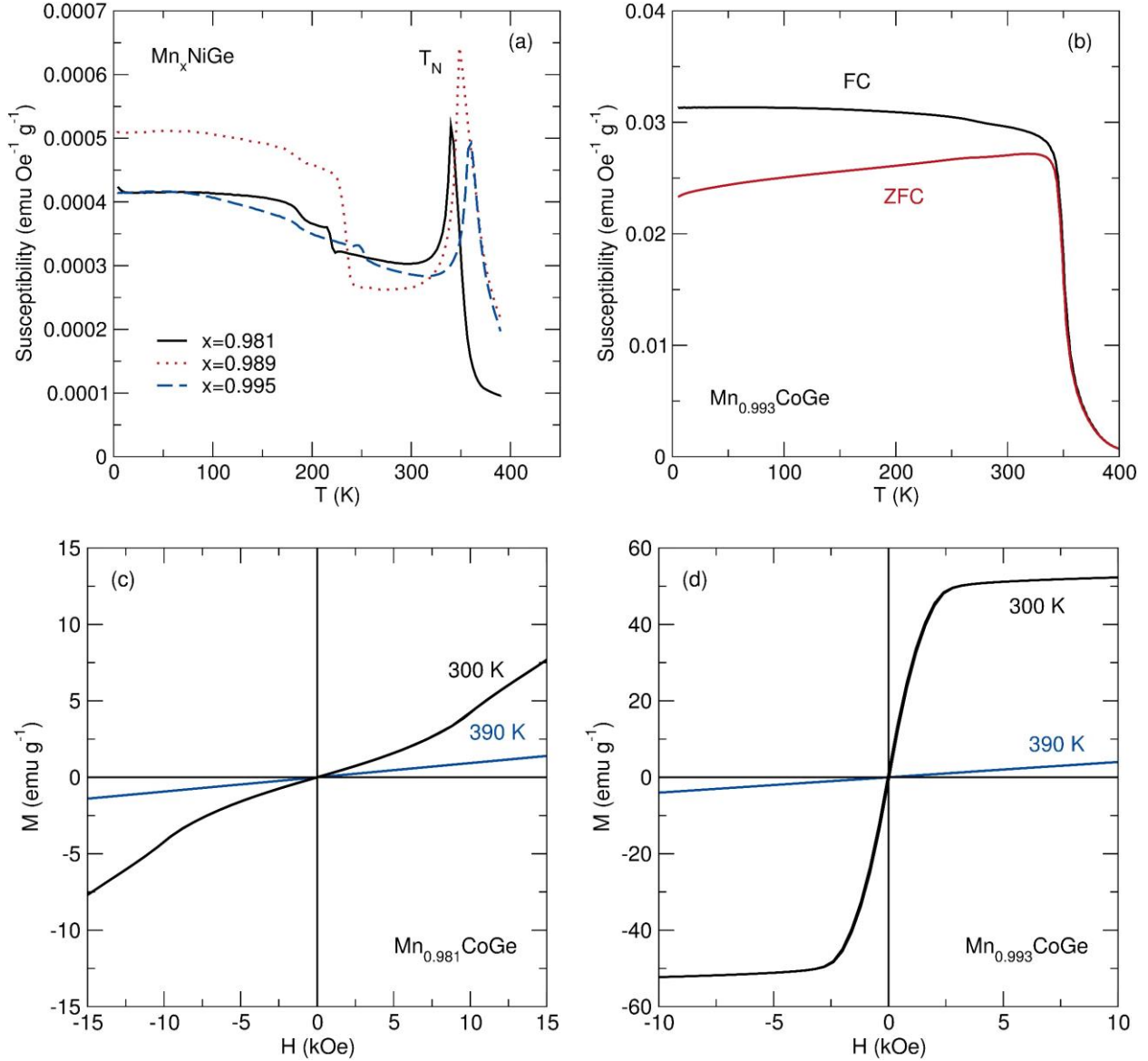
FIG. 4. Temperature dependence of the susceptibility of (a) Mn_xNiGe measured upon heating in 100 Oe field and (b) $Mn_{0.993}CoGe$ measured in field cooling (FC, black line) and zero field cooling (ZFC, red line) under 100 Oe applied field. M vs. H curve for (c) $Mn_{0.981}NiGe$ and (d) $Mn_{0.993}CoGe$ at 300 K (black line) and 390 K (blue line).

Representative data of the temperature-dependent magnetic susceptibility in the presence of 100 Oe magnetic field for Mn_xNiGe with $x = 0.981$, 0.989, and 0.995 are plotted in Fig. 4 (a). Field cooling and zero field cooling susceptibility of $Mn_{0.993}CoGe$ is demonstrated in Fig. 4(b). Upon cooling, the martensitic phase shows a magnetic transition from the paramagnetic (PM) state to

13

the antiferromagnetic (AFM) state at a Néel temperature T_N near 347 K (for stoichiometric MnNiGe) in agreement with previous studies [21,41,43]. The magnetic moments of 2.8 μ_B are localized on the Mn atoms and form an AFM spiral structure leading to a relatively low magnetization [43,44]. The step near ≈220 K corresponds to the AFM to AFM transformation from single to double spiral structure according to a previous neutron diffraction measurement [43]. The temperature dependent magnetization data of the $Mn_{0.993}CoGe$ (see Fig. 4(b)), by contrast, shows a PM to ferromagnetic (FM) transition upon cooling at a Curie temperature, T_c~350 K, in agreement with prior work [39]. We also performed measurement of magnetization vs. field (M vs. H) for $Mn_{0.981}NiGe$ and $Mn_{0.993}CoGe$ in (c) and (d) respectively. At 300 K, the magnetization of the $Mn_{0.981}NiGe$ shows antiferromagnetic behavior with a small kink on M at around 8 kOe which presumably corresponding to domain wall motion in polycrystalline antiferromagnets [45]. The M vs. H curve of $Mn_{0.993}CoGe$ at 300 K clearly shows the characteristic behavior of a ferromagnet with saturation at high fields. At 390 K, M vs. H curves for both $Mn_{0.981}NiGe$ and $Mn_{0.993}CoGe$ are linear, indicating they are paramagnetic.
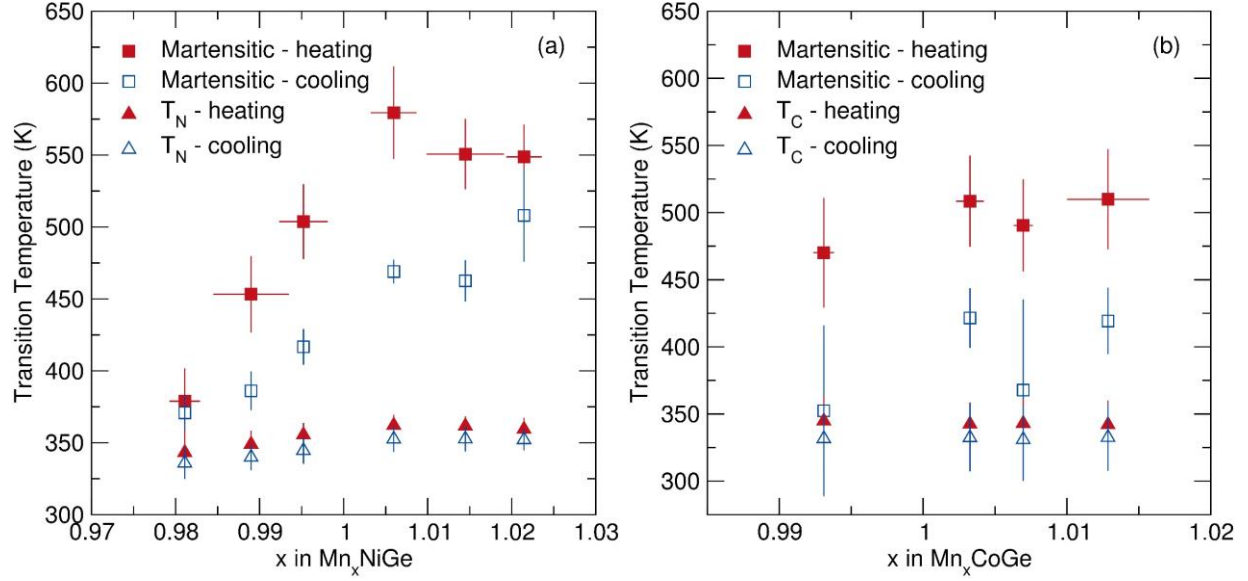
FIG. 5. The transition temperatures vs. Mn content of (a) Mn_xNiGe and (b) Mn_xCoGe samples determined by differential scanning calorimetry and X-ray fluorescence. The structural transition temperatures from the peak upon heating (red filled squares) and cooling (blue open squares) are shown and are directly related to the Mn composition. The standard deviation of the composition determined by four X-ray fluorescence data sets is the error bar for x (x-axis). The x-axis error bars were included only once for clarity since all the data points for the same sample (same x value) have equivalent error bars. The error bars for the temperature axis (y-axis) demonstrate the total width of the peak in DSC. Increasing the Mn content results in a plateau in the trend. The magnetic transition temperatures (i.e. Néel temperature T_N of Mn_xNiGe and Curie temperature T_C of Mn_xCoGe) upon heating (red filled triangles) and cooling (blue open triangles) are not sensitive to the Mn composition.

The transition temperature as a function of Mn content, x, in Mn_xMGe (M = Co, Ni) are summarized in Fig. 5. In Mn_xNiGe, the structural transition temperature is directly related to the Mn content for lower amounts of Mn. As the Mn content is increased past $x \approx 1.01$, the trend plateaus. A similar plateau is present in the lattice parameters for x greater than 1.01, as seen in Fig. 2. The similarity in these trends demonstrates the direct relationship between the crystal structure and structural transition temperature of the Mn_xNiGe system. In addition, the hysteresis between the peak in heating and cooling in thermal cycle becomes larger as x increases. The Mn_xNiGe transition temperatures range over ≈ 200 K. In contrast, the structural transition temperature of Mn_xCoGe is not highly dependent on the Mn content. As seen in Fig. 3 (b) and Fig.

5 (b), the transition temperatures are clustered around 500 K. The magnetic phase transition temperature in Mn_xMGe (M = Co, Ni) shows relatively small hysteresis upon heating and cooling and is not sensitive to the Mn content.
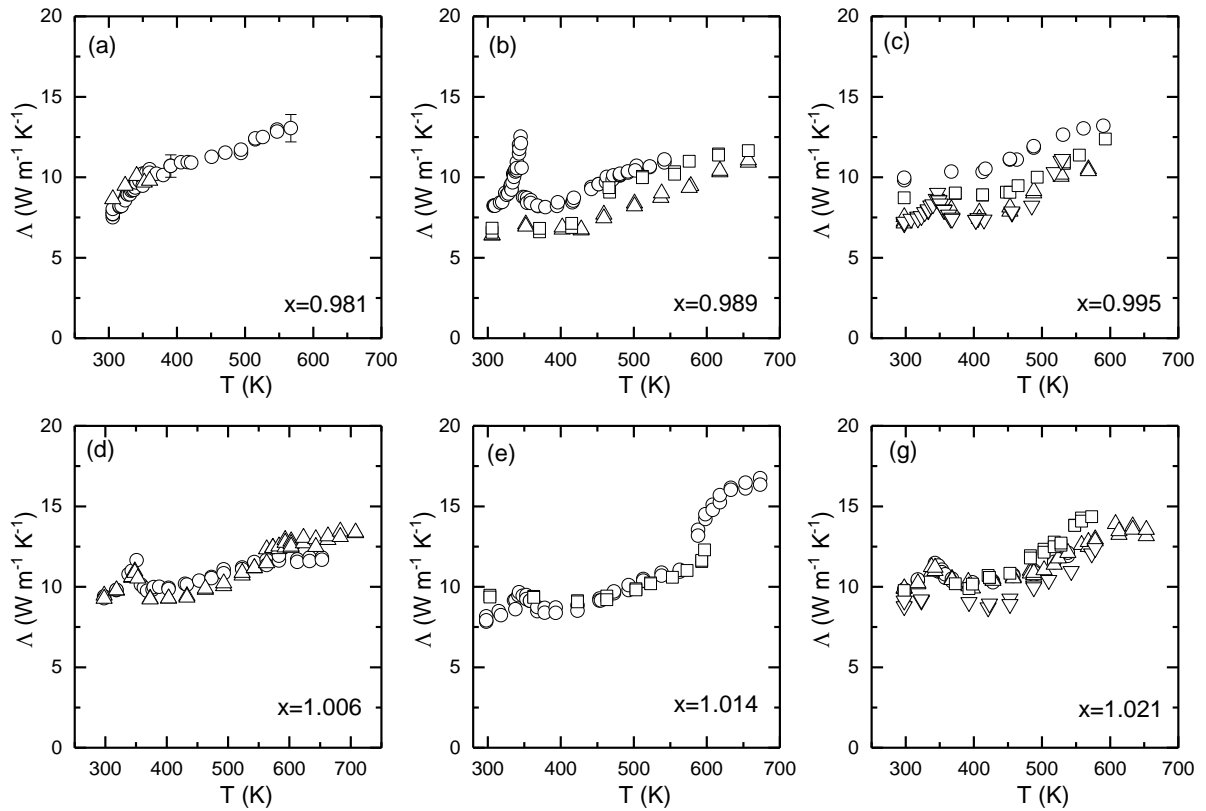

FIG. 6. Apparent thermal conductivity in Mn_xNiGe (x=0.981, 0.989, 0.995, 1.006, 1.014, and 1.021) from 300 K to 700 K. Each symbol type corresponds to measurements performed on different pieces from the same batch. The representative error bars are demonstrated in (a). Data near the magnetic phase transition around 350 K is not shown in all data to better demonstrate the overall thermal conductivity behavior through the martensitic transition.

We plot the temperature dependence of the thermal conductivity between 300 and 700 K of Mn_xNiGe in Fig. 6. TDTR measurements were performed on multiple pieces of the same sample. The pieces were not specifically oriented before polishing, so, presumably, a variety of

crystallographic orientations were probed. We attribute the scatter in the data for samples with the same composition to the anisotropy of the crystal in both the martensite (TiNiSi-type orthorhombic) and the austenite phase (Ni_2In-type hexagonal).

Upon heating from 300 K, a peak near 350 K appears corresponding to the sharp magnetic phase transition. Generally, for a bulk sample, TDTR is sensitive to the thermal effusivity of the sample, $(\Lambda C)^{1/2}$ and the heat capacity must be known to extract the thermal conductivity. For the data plotted in Fig. 6, as discussed above, we fixed C at a constant value. In reality, however, the heat capacity has a peak near the magnetic phase transition. If the temperature oscillation used in the TDTR measurement is larger than the hysteresis of the phase transition [15], the heat capacity peak will appear in the analyzed data as a peak in the thermal conductivity. We refer to the thermal conductivity analyzed using a constant heat capacity as the "apparent thermal conductivity". The magnetic transitions have small hysteresis and therefore the temperature oscillation caused by the modulated pump laser heating (0.3 K) are sensitive to the increases in the magnetic heat capacity near the magnetic transition. Hence, the change in the apparent thermal conductivity near the magnetic transition is likely due to the heat capacity change. There is nearly no change in thermal conductivity before and after the magnetic transition.

On the other hand, for a structural transition with significant hysteresis, the temperature oscillations caused by the laser heating are not large enough to trigger a local phase transition that can follow the rapid, temperature oscillation at 9.1 MHz frequency.

As the temperature increases further, the thermal conductivity increases monotonically. This rise in thermal conductivity corresponds to the broad martensitic structural transition with a relatively large hysteresis of nearly 100 K [46], which is sometimes observed in our thermal conductivity measured in TDTR (not shown). The polycrystalline samples tend to crack as they

are heated and cooled through the structural transition temperature due to the large strains produced by a 2.7% change in unit cell volume [21]. Thus, we could not reliably obtain a full thermal cycle of the TDTR measurements at each location of every sample.

In general, a higher Mn content, in addition to increasing the T_m, also enhances the magnitude of increase in thermal conductivity through the MT. The sharpest increase is observed in $Mn_{1.014}NiGe$ which changes by ~40% from ≈11 to ≈15.5 W m^{-1} K^{-1}, in 575 K< T < 625 K. (See Fig. 9 and the associated discussion for a quantitative summary of the fractional increases in thermal conductivity of Mn_xNiGe and comparisons between materials.) The inflection points of the step-like increase in the thermal conductivity data correspond to the T_m and are consistent with the DSC results. The relatively steep change of thermal conductivity in samples Mn_xNiGe with x = 1.014, and 1.021 in temperature upon heating are consistent with the narrower endothermic peaks in DSC in samples with higher Mn content.
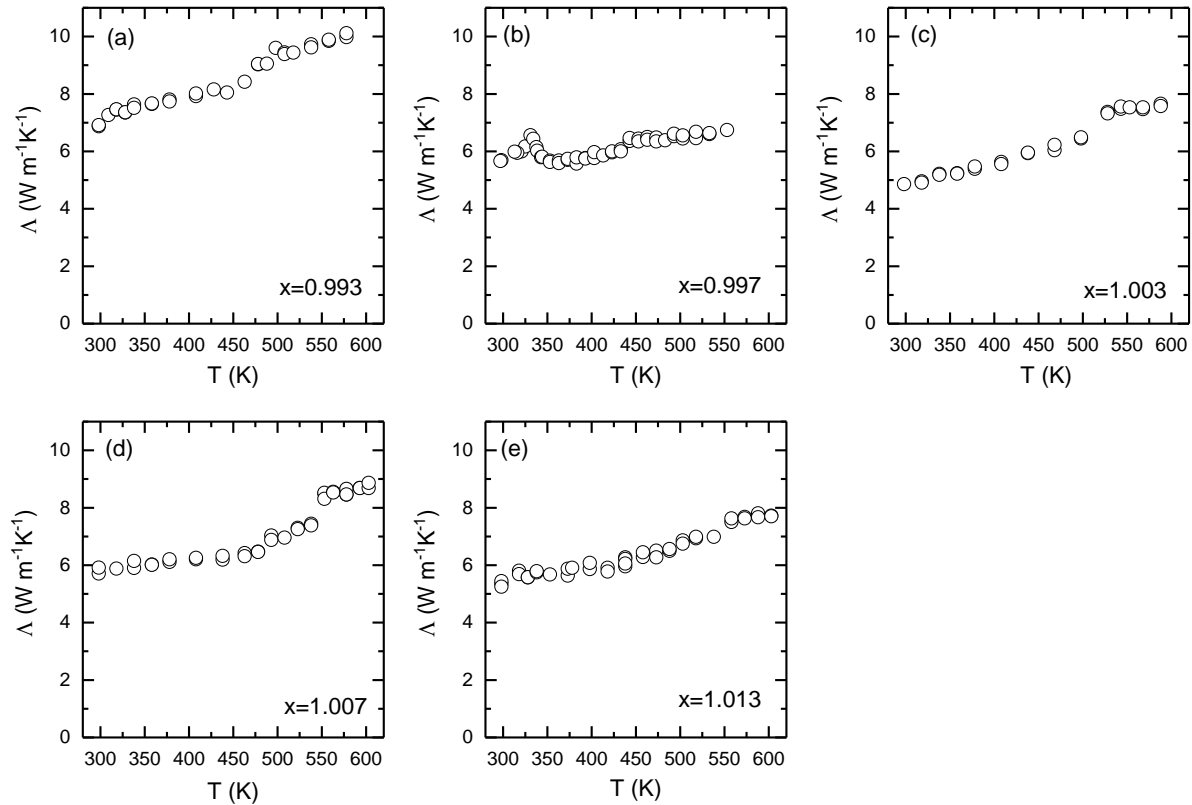
FIG. 7. Temperature dependence of apparent thermal conductivity in Mn_xCoGe ($x = 0.993$, 0.997, 1.003, 1.007, and 1.013) from 300 K to 600 K during heating.

As with the structural transition temperature (Fig. 3 (b)), the thermal conductivity anomaly of Mn_xCoGe is not highly dependent on the Mn content. Fig. 7 displays the temperature dependence of the thermal conductivity of Mn_xCoGe compounds during heating. In contrast to Mn_xNiGe, not all samples exhibit a prominent peak near 350 K of the Curie temperature except for $x = 0.997$ and 1.013. This suggests that the FM to PM magnetic transition is wide in temperature or has significant hysteresis. In all Mn_xCoGe samples, an increase in thermal conductivity corresponding to the broad martensitic structural transition is observed. The sharpest increase in thermal conductivity is observed in $Mn_{1.007}CoGe$ and $Mn_{1.003}CoGe$ which changes by $\approx$25-30% from 450 to 550 K. In other samples the change of thermal conductivity through the MT is between 7 and 20%.

Discussion

To better understand what drives the changes in the total thermal conductivity through the structural transition in Mn_xMGe, we must attempt to separate the contribution to the thermal conductivity from electrons and phonons. This is typically done by calculating the electronic thermal conductivity from electrical resistivity using the Wiedemann-Franz law [47]. Most of the Mn_xMGe samples in this study are small and irregularly-shaped with internal cracks, and therefore difficult to characterize with four-point-probe electrical conductivity measurements.

To evaluate the room temperature electrical resistivity of these alloys, we instead performed infrared spectroscopy on polished $Mn_{1.007}CoGe$ and $Mn_{1.006}NiGe$ samples and analyzed the reflectance spectra from 1000 to 7500 cm^{-1} using a Lorentz-Drude (LD) model, following

references [48,49]. In this model, the complex dielectric function is expressed as: $\varepsilon_r(\omega) = \varepsilon_r^{(f)}(\omega) + \varepsilon_r^{(b)}(\omega)$, which separates explicitly the intraband electron transition effect (free-electron effect) from interband electron transition effects (bound electron effect). The intraband part of the dielectric function, $\varepsilon_r^{(f)}(\omega)$, is described by the free-electron Drude model

$$\varepsilon_r^{(f)}(\omega) = 1 - \frac{\omega_p^2}{\omega(\omega - i\Gamma_0)},$$ where $\omega_p^2 = ne^2/m^*\varepsilon_0$ is the plasma frequency, in which e is the charge of the electron, m^* is electron effective mass, n is the number of free electrons per unit volume and ε_0 is the vacuum permittivity; $\Gamma_0 = 1/\tau$ is the carrier scattering rate with τ being the relaxation time. The interband part $\varepsilon_r^{(b)}(\omega)$ is described as k Lorentz oscillators

$$\varepsilon_r^{(b)}(\omega) = \sum_{j=1}^{k} \frac{\omega_{pj}^2}{(\omega_j^2 - \omega^2) + i\omega\Gamma_j},$$ centered at ω_j with plasma frequency ω_{pj}, and damping rate Γ_j.

Such a model has been applied to a series of metals and alloys to estimate their electrical conductivity, giving reasonable results compared with DC measurements [50-52]. We consider only one bound electron term in the LD model and use the model to fit our experimental spectra by adjusting the five parameters of ω_p, Γ_0, ω_j, ω_{pj}, and Γ_j. The electrical conductivity is then estimated from $\sigma_0 = \varepsilon_0\omega_p^2/\Gamma_0$.
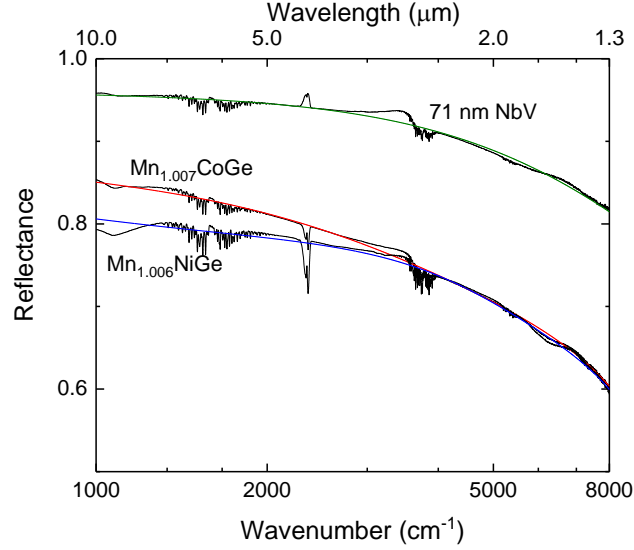
FIG. 8 Infrared reflectance of $Mn_{1.007}CoGe$ and $Mn_{1.006}NiGe$ compared with Lorentz-Drude model fitting. The data for 71 nm NbV film on Si wafer and the corresponding model fitting are also included for comparison.

In Fig. 8, we plot the measured IR reflectance of $Mn_{1.007}CoGe$ and $Mn_{1.006}NiGe$ in comparison with Lorentz-Drude model fitting results. (See Table 1 for the fitting parameters.) The free electron and bound electron parts of the dielectric function show different wavelength dependence, see Fig. S3. Hence, the fitting parameters of ω_p and Γ_0 are relatively independent of the other three parameters for the bound electron term. We do not try to fit the weak local features from the instrument ($\sim$1050 cm^{-1} and $\sim$3500 cm^{-1}) and absorption band of H_2O ($\sim$1600 cm^{-1} and $\sim$3600 cm^{-1}) and CO_2 ($\sim$2350 cm^{-1}). The 300 K electrical resistivity of the $Mn_{1.007}CoGe$ and $Mn_{1.006}NiGe$ are measured to be 470 and 680 $\mu\Omega$ cm, respectively which are lower than some $Mn_{1-x}Fe_xNiGe$ alloys but higher than Ni-Mn-In and Ni_2MnGa alloys reported in the literature [30,39,53,54]. Such resistivities correspond to electronic thermal conductivities of 1.6 W m^{-1} K^{-1} for $Mn_{1.007}CoGe$ and 1.1 W m^{-1} K^{-1} for $Mn_{1.006}NiGe$ at 300 K, small compared to their total thermal conductivities of approximately 6 and 9 W m^{-1} K^{-1}, respectively.

TABLE 1. Parameters used in the Lorentz-Drude model to fit the infrared reflectance of
$Mn_{1.007}CoGe$, $Mn_{1.006}NiGe$ and NbV in Fig. 8.

Sample	ω_p (cm^{-1})	Γ_0 (cm^{-1})	ω_{P1} (cm^{-1})	ω_1 (cm^{-1})	Γ_1 (cm^{-1})
$Mn_{1.007}CoGe$	9529	718	6485	1915	5821
$Mn_{1.006}NiGe$	10529	1287	3435	5762	7554
NbV	22898	492	20488	801	19178

We used a 71 nm NbV alloy thin film on Si wafer grown by magnetron sputtering as a convenient test sample to validate the measurement approach. The electrical resistivity obtained from the LD model for NbV is 55 µΩ cm, 15% higher than the value of 48 µΩ cm that we measured with a four-point probe method. Thus, we estimate the error in the electrical resistivity of the Mn_xMGe from the optical method to be around 15-18% considering the error from measurement and curve fitting.

We also measured the relative change of electrical conductivity in the polished sample of $Mn_{1.007}CoGe$ using the four-probe method. Although the sample thickness was not uniform enough to obtain the absolute value of electrical resistivity, we observed a ~20% decrease in electrical resistivity upon heating across around ≈500 K in a ≈50 K temperature range. Since the electrical resistivity keeps increasing with temperature, this suggests the change of the electronic contribution is <0.5 W m^{-1} K^{-1} which is smaller than the observed change of ~1.5 W m^{-1} K^{-1} in the total thermal conductivity through the MT in this sample. In alloys with martensitic transition, such as NiTi, Ni-Mn-In and Ni_2MnGa, the change of resistivity across the MT is typically less than 50% [27,30,32,33]. Thus, we believe the change in phonon thermal conductivity through the MT is important in the change of the total thermal conductivity for Mn_xNiGe and Mn_xCoGe. Such

results are different from the cases of Ni-Mn-In and Ni_2MnGa Heusler alloys where the change of electronic contribution dominates the change of total thermal conductivity [30,32,33].

The change of phonon dispersion when the Mn_xMGe samples transform between orthorhombic and hexagonal structure may be part of the reason for the change in phonon thermal conductivity. In addition, the higher density of twin boundaries may increase the phonon scattering rate at in the martensite phase and reduce the lattice thermal conductivity in Mn_xMGe alloys [55]. The change of phonon scattering by electrons through the MT may also play a role.

To evaluate the MT-induced thermal conductivity change of Mn_xMGe (M = Co, Ni) alloys for thermal regulator applications, we define an average logarithmic rate of change in thermal conductivity in a certain temperature range as: $Z = \dfrac{\partial \ln \Lambda}{\partial \ln T}$. The larger the absolute value of Z the faster the change in thermal conductivity. For materials with phase transitions, we calculated the average value of $\langle Z \rangle = \left\langle \dfrac{\partial \ln \Lambda}{\partial \ln T} \right\rangle \approx \left\langle \dfrac{T}{\Lambda} \dfrac{\Delta \Lambda}{\Delta T} \right\rangle$ in the range of approximately $T^* \pm 25$ K, where T^* is their correponding phase transition temperature. The data of $\langle Z \rangle$ for Mn_xMGe (M = Ni, Co) alloys, and $Z(T)$ and $\langle Z \rangle$ for some common materials between 300 to 600 K are compared in Fig. 9 including metals (Cu [56], 304 stainless steel [57], Ni-22 at% Cr alloy [58]), dielectrics (Si [5], SiO_2 [59], and natural type-IIa diamond [60]), NiTi alloys (this work and [27]), Ni-Mn-In alloys [17,32], Ni_2MnGa [30], $La_{0.35}Ca_{0.65}MnO_3$ [13], and VO_2 [15,18]. The largest value of $\langle Z \rangle$ is used if multiple data sets exist.

Above 300K, the Z value of common dielectrics and metals is typically negative while alloys have positive Z. Phase transition materials have noticeably larger $\langle Z \rangle$ correponding to a sharp change of thermal conductivity near their transition temperature. On average, among MT materials,

23

Z for Mn_xNiGe is larger than that for NiTi and Ni_2MnGa but smaller than that of Ni-Mn-In alloys. However, the martensitic phase transition in the latter typically occurs at a temperature below 300 K in literature. Mn_xCoGe shows smaller rate of change in thermal conductivity with $\langle Z \rangle$ comparable with NiTi. The largest value of $\langle Z \rangle$ is ≈ 2.5 for $Mn_{1.014}NiGe$ which means a 10% change in temperature would lead to 25% change in thermal conductivity near 550 K. Compared with MIT materials, $\langle Z \rangle$ for Mn_xMGe are comparable with that of $La_{0.35}Ca_{0.65}MnO_3$ but smaller than that of VO_2 thin film. As shown in Fig. 9, most of these phase transitions that lead to change in thermal conductivity in literature occurs at $T < 400$ K, lower than MT temperatures of Mn_xMGe alloys. The high temperature austenite phase thermal conductivity of Mn_xNiGe is 11 to 16 W m^{-1} K^{-1}, which is more than twice that of VO_2 and comparable to some of the aluminum alloys used in internal combustion engines [34].

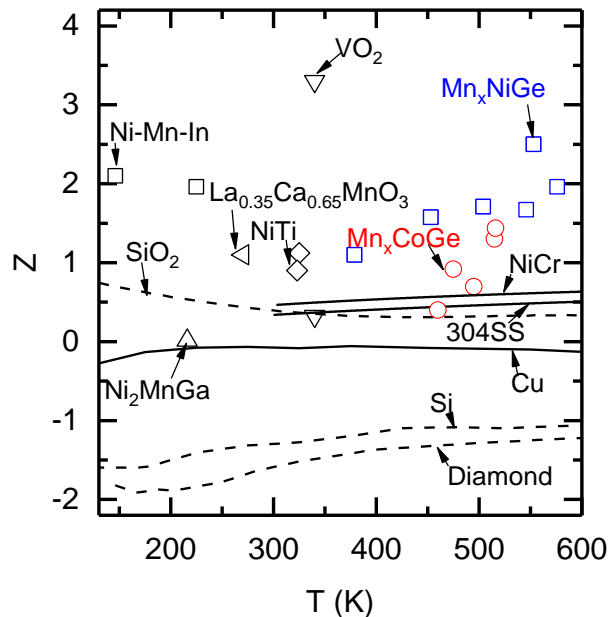FIG. 9. Average logarithmic rate of change in thermal conductivity Z defined in the main text of Mn_xNiGe (blue open squares), Mn_xCoGe (red open circles), Cu [56], 304 stainless steel [57], Ni-

22 at% Cr alloy [58], Si [61], SiO$_2$ [59], natural type-IIa diamond [60], NiTi alloys (this work and [27]), Ni-Mn-In alloys [17,32], Ni$_2$MnGa [30], La$_{0.35}$Ca$_{0.65}$MnO$_3$ [13], and VO$_2$ [15,18].

Conclusion

We measured the thermal conductivity as a function of temperature through the magnetic and martensitic phase transition in the Mn$_x$MGe (M = Co, Ni, $0.98 < x < 1.02$) alloys from 300 to 600 K using time-domain thermoreflectance. Through the martensitic transition, the rate of increase in thermal conductivity in these materials as a function of temperature is comparable or faster than several common metals alloys, NiTi and Ni$_2$MnGa. The most rapid increases are observed in Mn$_{1.014}$NiGe as 11 to 15.5 W m^{-1} K^{-1} and Mn$_{1.007}$CoGe as $\approx$7 to $\approx$8.5W m^{-1} K^{-1}. The martensitic transition temperature and the thermal conductivity change are sensitive to the composition of Mn in Mn$_x$NiGe. The change in the total thermal conductivity is largely from the change in the phonon contribution in Mn$_x$MGe. This work extends the scope of thermal regulating materials exhibiting a temperature-induced transition with higher thermal conductivity in the high temperature phase.

Acknowledgement

[1]   J. B. Heywood, *Internal combustion engine fundamentals* (Mcgraw-hill New York, 1988), Vol. 930.

[2]   F. Will and A. Boretti, SAE International Journal of Engines **4**, 175 (2011).

[3]   R. Cipollone, D. Di Battista, and M. Mauriello, Energy Procedia **82**, 1 (2015).

[4]   D. G. Cahill, W. K. Ford, K. E. Goodson, G. D. Mahan, A. Majumdar, H. J. Maris, R. Merlin, and S. R. Phillpot, Journal of Applied Physics **93**, 793 (2003).

[5]   C. J. Glassbrenner and G. A. Slack, Physical Review **134**, A1058 (1964).

[6]   D. R. Clarke, Surface and Coatings Technology **163**, 67 (2003).

[7]   W. S. Williams, JOM Journal of the Minerals, Metals and Materials Society **50**, 62 (1998).

[8]   G. Welsch, R. Boyer, and E. W. Collings, *Materials Properties Handbook: Titanium Alloys* (ASM International, 1993).

[9]   L. G. Radosevich and W. S. Williams, Physical Review **181**, 1110 (1969).

[10]   Q. Zheng, A. B. Mei, M. Tuteja, D. G. Sangiovanni, L. Hultman, I. Petrov, J. E. Greene, and D. G. Cahill, Physical Review Materials **1**, 065002 (2017).

[11]   S. Gratch, *Advances in Thermophysical Properties at Extreme Temperatures and Pressures: Papers Presented at Third Symposium on Thermophysical Properties, Purdue University, Lafayette, Indiana, March 22-25, 1965* (American Society of Mechanical Engineers, 1965).

[12]   M. K. Hooda and C. S. Yadav, Physica B: Condensed Matter **491**, 31 (2016).

[13]   J. Cohn, J. Neumeier, C. Popoviciu, K. McClellan, and T. Leventouri, Physical Review B **56**, R8495 (1997).

[14]   A. J M Honig and L. L. V. Zandt, Annual Review of Materials Science **5**, 225 (1975).

[15]   D.-W. Oh, C. Ko, S. Ramanathan, and D. G. Cahill, Applied Physics Letters **96**, 151906 (2010).

[16]   A. Mineshige, M. Inaba, T. Yao, Z. Ogumi, K. Kikuchi, and M. Kawase, Journal of Solid State Chemistry **121**, 423 (1996).

[17]   B. Zhang, X. X. Zhang, S. Y. Yu, J. L. Chen, Z. X. Cao, and G. H. Wu, Applied Physics Letters **91**, 012510 (2007).

[18]   S. Lee, K. Hippalgonkar, F. Yang, J. Hong, C. Ko, J. Suh, K. Liu, K. Wang, J. J. Urban, X. Zhang, C. Dames, S. A. Hartnoll, O. Delaire, and J. Wu, Science **355**, 371 (2017).

[19]   A. Jain, S. P. Ong, G. Hautier, W. Chen, W. D. Richards, S. Dacek, S. Cholia, D. Gunter, D. Skinner, G. Ceder, and K. A. Persson, APL Materials **1**, 011002 (2013).

[20]   Y.-Y. Zhao, F.-X. Hu, L.-F. Bao, J. Wang, H. Wu, Q.-Z. Huang, R.-R. Wu, Y. Liu, F.-R. She, H. Kuang, M. Zhang, W.-L. Zuo, X.-Q. Zheng, J. R. Sun, and B.-G. Shen, J. Am. Chem. Soc **137**, 1746 (2015).

[21]   E. Liu, W. Wang, L. Feng, W. Zhu, G. Li, J. Chen, H. Zhang, G. Wu, C. Jiang, H. Xu, and F. de Boer, Nat Commun **3**, 873 (2012).

[22]   L. Caron, N. T. Trung, and E. Brück, Physical Review B **84**, 020414 (2011).

[23]   V. Johnson, Inorganic Chemistry **14**, 1117 (1975).

[24]   S. Nizioł, A. Wesełucha, W. Bażela, and A. Szytuła, Solid State Communications **39**, 1081 (1981).

[25]   S. Zhu, M. Ye, K. Shirai, M. Taniguchi, S. Ueda, Y. Miura, M. Shirai, R. Y. Umetsu, R. Kainuma, T. Kanomata, and A. Kumura, Journal of Physics: Condensed Matter **27**, 362201 (2015).

[26]   M. Ye, A. Kumura, M. M. Shirai, Y. T. Cui, K. Shimada, H. Namatame, M. Taniguchi, S. Ueda, K. Kobayashi, R. Kainuma, T. Shishido, K. Fukushima, and T. Kanomata, Physical Review Letters **104**, [27] B. D. Ingale, W. C. Wei, P. C. Chang, Y. K. Kuo, and S. K. Wu, Journal of Applied Physics **110**, 113721 (2011).

[28]   S. Y. Yu, Z. H. Liu, G. D. Liu, J. L. Chen, Z. X. Cao, G. H. Wu, B. Zhang, and X. X. Zhang, Applied Physics Letters **89**, 162503 (2006).

[29]   R. Barman, S. K. Singh, and D. Kaur, Current Applied Physics **14**, 1755 (2014).

[30]   Y. Kuo, K. Sivakumar, H. Chen, J. Su, and C.-S. Lue, Physical Review B **72**, 054116 (2005).

[31]   L. S. Chandra, M. Chattopadhyay, V. Sharma, S. Roy, and S. K. Pandey, Physical Review B **81**, 195105 (2010).

[32]   A. Batdalov, A. Aliev, L. Khanov, V. Buchel'nikov, V. Sokolovskii, V. Koledov, V. Shavrov, A. Mashirov, and E. Dil'mieva, Journal of Experimental and Theoretical Physics **122**, 874 (2016).

[33]   B. Zhang, X. Zhang, S. Yu, J. Chen, Z. Cao, and G. Wu, Applied Physics Letters **91**, 012510 (2007).

[34]   E. Buyukkaya, Surface and Coatings Technology **202**, 3856 (2008).

[35]   D. G. Cahill, Review of Scientific Instruments **75**, 5119 (2004).

[36]   K. Kang, Y. K. Koh, C. Chiritescu, X. Zheng, and D. G. Cahill, Review of Scientific Instruments **79**, 114901 (2008).

[37]   D. G. Cahill and F. Watanabe, Physical Review B **70**, 235322 (2004).

[38]   E. H. Buyco and F. E. Davis, Journal of Chemical & Engineering Data **15**, 518 (1970).

[39]   T. Samanta, I. Dubenko, A. Quetz, J. Prestigiacomo, P. W. Adams, S. Stadler, and N. Ali, Applied Physics Letters **103**, 042408 (2013).

[40]   P. Markin, N. Mushnikov, A. Proshkin, and S. Belyaev, in *Solid State Phenomena* (Trans Tech Publ, 2012), pp. 331.

[41]   W. Bazela, A. Szytuła, J. Todorović, Z. Tomkowicz, and A. Zięba, physica status solidi (a) **38**, 721 (1976).

[42]   E. K. Liu, H. G. Zhang, G. Z. Xu, X. M. Zhang, R. S. Ma, W. H. Wang, J. L. Chen, H. W. Zhang, G. H. Wu, L. Feng, and X. X. Zhang, Applied Physics Letters **102**, 122405 (2013).

[43]   H. Fjellvåg and A. F. Andresen, Journal of Magnetism and Magnetic Materials **50**, 291 (1985).

[44]   B. D. Cullity and C. D. Graham, *Introduction to Magnetic Materials* (John Wiley & Sons, 2011).

[45]   D. Bloch, J. L. Feron, R. Georges, and I. S. Jacobs, Journal of Applied Physics **38**, 1474 (1967).

[46]   V. V. Kokorin, V. V. Koledov, V. G. Shavrov, S. M. Konoplyuk, S. Thürer, D. A. Troyanovsky, H. J. Maier, and V. V. Khovaylo, Journal of Applied Physics **116**, 103515 (2014).

[47]   R. Franz and G. Wiedemann, Annalen der Physik **165**, 497 (1853).

[48]   A. D. Rakić, A. B. Djurišić, J. M. Elazar, and M. L. Majewski, Applied Optics **37**, 5271 (1998).

[49]   H. Ehrenreich, H. Philipp, and B. Segall, Physical Review **132**, 1918 (1963).

[50]   L. Schulz, Journal of the Optical Socity of America **44**, 540 (1954).

[51]   S. Dordevic, D. Basov, A. Ślebarski, M. Maple, and L. Degiorgi, Physical Review B **66**, 075122 (2002).

[52]   Y. Zhou, X. Jin, H. Xu, Y. Kudryavtsev, Y. Lee, and J. Rhee, Journal of Applied Physics **91**, 9894 (2002).

[53]   P. Dutta, S. Pramanick, V. Singh, D. T. Major, D. Das, and S. Chatterjee, Physical Review B **93**, 134408 (2016).

[54]   B. M. Wang, L. Wang, Y. Liu, B. C. Zhao, Y. Zhao, Y. Yang, and H. Zhang, Journal of Applied Physics **106**, 063909 (2009).

[55]   S. Bhattacharya, M. J. Skove, M. Russell, T. M. Tritt, Y. Xia, V. Ponnambalam, S. J. Poon, and N. Thadhani, Physical Review B **77**, 184203 (2008).

[56]   W. M. Haynes, *CRC Handbook of Chemistry and Physics, 96th Edition* (CRC Press, 2015).

[57]   R. S. Graves, T. G. Kollie, D. L. McElroy, and K. E. Gilchrist, International Journal of Thermophysics **12**, 409 (1991).

[58]   R. Endo, M. Shima, and M. Susa, International Journal of Thermophysics **31**, 1991 (2010).

[59]   D. G. Cahill, Review of Scientific Instruments **61**, 802 (1990).

[60]   J. R. Olson, R. O. Pohl, J. W. Vandersande, A. Zoltan, T. R. Anthony, and W. F. Banholzer, Physical Review B **47**, 14850 (1993).

[61]   W. Fulkerson, J. P. Moore, R. K. Williams, R. S. Graves, and D. L. McElroy, Physical Review **167**, 765 (1968).